The design of an impact-resistant drivetrain for a robotic ball

Bart Horstman

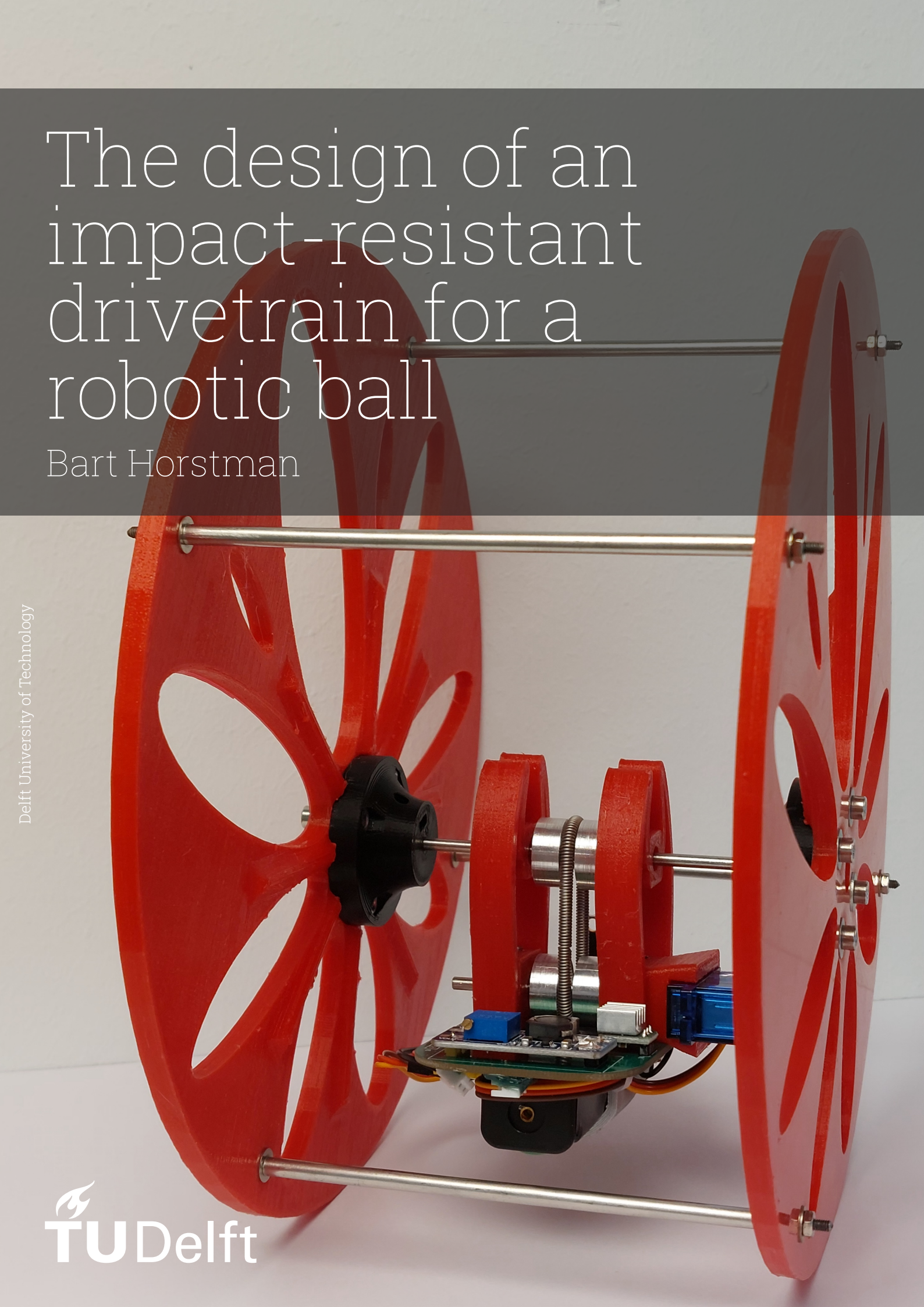

Delft University of Technology

TU Delft

Preface

Enhancing mobility has always fascinated me, together with a mechanical design aspect becomes a great motivator. Therefore, I'm grateful for this master thesis project and hopefully stimulate movement with the design made.

My thesis could not have worked without the help of my two supervisors, Heike Vallery and Marco Rozendaal. I would like to thank them both for their insights and feedback. Despite the difficulty of scheduling a meeting with them together, it was motivating to see how they balanced a good mixture of creativity and functional design.

Last year Heike introduced me to Giuseppe Radaelli. The meetings with Giuseppe were very helpful and would like to thank him for taking the time for my questions. Heike also introduced me to the DBL lab, which got me a new workplace, friends, and the organization of a cleanup day. I would like to express my gratitude to the people in the lab and a special thanks to Bob for the short feedback moments and fun in the office.

Lastly, I would like to thank my parents for their support and I would like to thank my girlfriend who can cheer me up as well as tell me to get to work and will always be in my mind.

Bart Horstman
Delft, August 2023

ME51010-20 ME BMD Master thesis report
B.E. Horstman, Delft, The Netherlands, compiled August 18, 2023

The design of an impact-resistant drivetrain for a robotic ball

Bart Horstman

***Abstract*—This study introduces a new design for the drivetrain of a robotic ball. An application for the robotic ball is a rehabilitation device for young children. With these children, movement can be stimulated in a more intuitive way when a robotic ball is used compared to other training programs. Since the ball will be kicked and played with, an important requirement is the ability to handle multiple impacts, i.e. the ball is impact resistant. Additional requirements are the ability to roll like a normal ball (the center of gravity is in the center of the ball) and maintain low weight and cost. The final design is found through iterative testing and shape optimization of the individual components. The impact resistance of the final design is met by protecting from torque overload and the possibility to absorb shocks, however, the latter still requires testing to confirm the drivetrain's impact resistance. The proposed design successfully fulfills the size and weight requirements for implementation in a robotic ball, representing a promising step toward creating a robotic ball with enhanced impact resistance. A subject for future research remains the development of the complete robotic ball, with a shell and suspension mechanism.**

I. Introduction

A. Motivation

Maintaining regular exercise and learning basic motor skills are essential for the development of young children [1] [2] [3]. However, it can be restricted when children are forced to be in hospitals or immobilized in bed due to their illness or injury. Exercise programs are in place, but focus on predetermined movements and include screen time [4]. A more intuitive way is proposed by a company called Luuno in collaboration with the Delft Technical University and Erasmus Medical Institute. The aim is to let the children interact with the environment and stimulate movement by using a robotic ball, named Fizzy.

The current design of Fizzy has similar characteristics to commercial alternatives, where the movement is generated with an off-center moving mass and the outer shell is rigid. A difference is the application of these commercial balls, for example, the GroundBot (Rotundus AB, Sweden) [5] is used in surveillance. The Wicked Ball SE (Cheerble, USA) [6] is used for pets and the Sphero BOLT (Sphero Inc. USA) [7] is used as educational tool. The latter has also been used in studies to test the effect a robotic ball has on children's behaviour [8] [9]. The study's preliminary results are in favor of using a spherical robot, however, further research is required with larger group sizes. Another study with a noncommercial ball, Roball [10], also indicates improvements in mobility through a spherical robot [11]. These studies show the potential of a robotic ball being used for rehabilitation. The hypothesis is that with a new robotic ball design the interaction with the children will be enhanced, which together with a cost-effective design could result in a promising solution for a new rehabilitation toy.

Literature reviews already show multiple design options and sensors that can be used in robotic balls [12] [13] [14]. The proposed design for Fizzy differs from the state of the art in multiple aspects. The first is the use of only one motor to accommodate all movement directions. Second, the axis around which the moving mass is rotating is not in the center of the ball. This will enable the ball to have a 'folded' position with the center of mass in the middle of the sphere (Fig. 1). Third, the electronics are used as moving mass, making the whole system lighter by not having to add additional weights. And lastly, the shell of the ball will be deformable, like a normal soccer ball. The deformable shell and the interaction with children impose an important requirement on the internal mechanism of the ball, namely being capable of handling multiple impacts. The need for an impact-resistant drivetrain becomes clear.

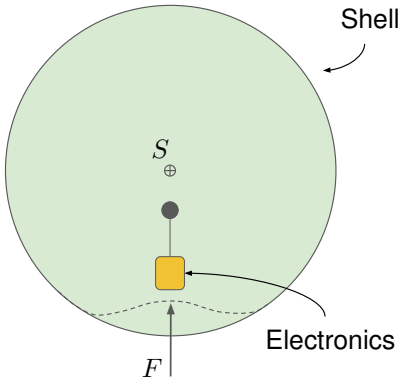

Fig. 1. Proposed mechanical layout of the new Prototype of Fizzy. The robotic ball has a deformable shell with electronics inside connected to an axis that has an off-set with the center of the ball S. The shell can transfer impact force F to the electronics under certain loads.

B. Impact scenarios

The drivetrain, including the motor, transmission, and electronics is exposed to the impact a child can impose on the robotic ball. This study considers two worst-case impact scenarios. The first scenario is a fast deceleration of the complete drivetrain, with critical stresses on the motor axis and connection points (Fig. 2(a)). Conventional options to include a buffer layer between the impacting surface and the component that needs protecting can not be applied in this case. The reason is the limited amount of space (weight close to the surface) and weight-saving requirement.

For the second scenario, the drivetrain is horizontal with respect to the fixed axis around which it can rotate. When the ball hits an object in this configuration, the motor axis

The author is a master's student at the Faculty of Mechanical, Maritime and Materials Engineering, Technical University Delft. b.e.horstman@student.tudelft.nl

and with it the transmission from the motor is exposed to a critical torque (Fig. 2(b)).

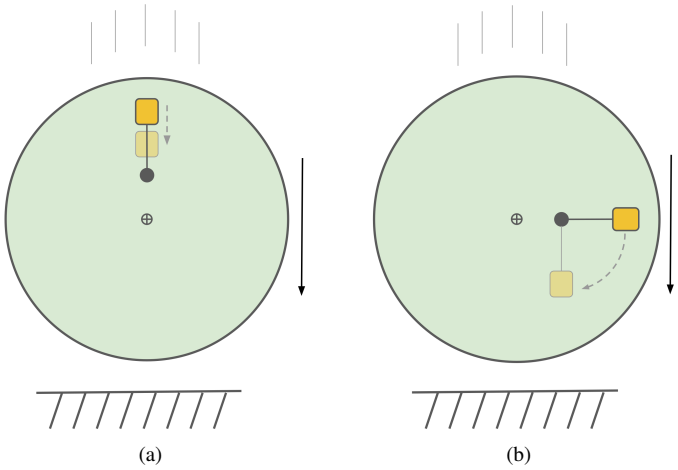

Fig. 2. Two different impact scenarios. (a) Fast deceleration, where the shock is absorbed through the structural connections. (b) Torque overload, with critical torque on the motor axis.

C. Robust drivetrain

The state of the art in impact-resistant drive trains can also be divided into the previously mentioned impact scenarios shock absorption and torque overload. Shock absorption can most efficiently be achieved by a system that exerts a constant force while displaced, e.g. the crumple zone of a car [15]. More information on constant force mechanisms is given in Appendix A. Examples of advanced suspension systems that use constant force mechanisms are found in a gravity compensator [16] or in the landing gear on a Mars rover [17]. In the case of the gravity compensator, the suspension system is limited by the need for an active system. An active suspension system can not be implemented in small designs that require low battery usage. The landing system of the Mars rover fixes this problem by being passive. However, the compactness of this design is low. Defining compactness as the stroke length divided by the build-in height. A solution with higher compactness has the potential to absorb more energy and reduce weight.

Instead of a mechanical mechanism a material layer can also be used as an energy absorber. Examples are the padding of a shin guard, the rubber casing of a mobile phone, or the more advanced metamaterial as proposed by Yang and Ma [18]. General impact absorbing systems use a spring-damper system together with rigid components to guide the movement, e.g. the four-bar linkages design in cars. Impact mitigation with only an impact-absorbing material layer solves this problem. However, the amount of material needed to replace the structural properties of the guiding system make the design big and heavy. Therefore, the layered materials that absorb impact do not suffice in a minimal-weight design. Metamaterials are lighter compared to solid material layers but have a limited stroke compared to their size, i.e. low compactness.

The protection for torque overload can be solved by a torque limiter. Examples of torque limiters are a shear pin, friction coupling [19] [20], a tolerance ring [21] [22], hydraulic coupling [23], ball-detent coupling [24] or magnetic coupling [25] [26]. The main limitation of current torque limiters is the added length to the motor axis. A shear pin is an exception in this case but needs replacement after the first impact. Since space is limited inside a robotic ball the added length with the torque limiter is not desirable.

A solution that does not add extra components to the drivetrain is a direct drive motor or the use of a low inertia gearbox. The inertia of a gearbox is coupled with the transmission ratio, a lower transmission ratio means lower inertia. The MIT cheetah design is an example of a low-geared system (gear ratio of 1:5.8) [27]. The drivetrain is highly backdrivable and has the advantage of a high control bandwidth. When impacted the inertia of the drivetrain is low enough to mitigate the acceleration force imposed on the gears. The use of highly backdrivable joints is not only seen in robot dogs but also in the field of exoskeletons [28] [29] and robotic devices interacting with humans [30] [31]. The downside of a low-geared motor is the need for a high-torque motor in order to meet the torque requirements. High-torque motors are big, heavy, and costly, compared to traditional geared motors. Another factor that needs consideration is the power consumption of the motor. With a highly backdrivable drivetrain a constant energy consumption is required to hold the desired position.

D. Design objective

An impact-resistant drivetrain that can be implemented in a robotic ball and meets the requirements of Fizzy, has not presented itself in literature. The shock-absorbing solutions are either too heavy, bulky, costly, or require continuous power. The same holds for the solutions for torque overload, as the proposed designs add extra weight, costs, or length to the system. Therefore, the following design objective is set for this study: *design a drivetrain that is resistant to torque overload and peak deceleration and meets the design requirements of the robotic ball, Fizzy.*

With an impact-resistant drivetrain, Fizzy can be made more reliable and sustainable. The design can last longer with the shock absorption protecting the internal mechanism and can give a new look upon the use of robotic devices in rehabilitation, or in general in toys.

The proposed design is constructed by first setting up the requirements, which are shown in Section II-A. From these requirements, a design is proposed with the working principle and the shape optimization explained in Sections II-B and II-C respectively. The tests and test setup that are required to validate the proposed design are shown in Section II-D. Section III holds the result from the tests as well as the final design configuration. Lastly, a review of the performance of the design and concluding take-home message is found in Sections IV and V.

II. Methods

A. Requirements

1) Fizzy: The requirements for the design of Fizzy are based on the dimensions of a soccer ball and the specifications of the previous prototype of Fizzy. The restriction on the total weight and size is similar to an official youth soccer ball, 400 g and a diameter of 200 mm.

Fig. 3 shows an overview of the layout and the dimensions of the system. The internal mechanism consists of an axis that is fixed to the shell (A). The axis has an offset (a) from the center of the sphere (S). The electronics that rotate around the fixed axis have a center of gravity (D) and the distance to the fixed axis and sphere center are (b) and (c) respectively. Length (c) should not be larger than 70 mm, taking into account a 5 mm thick shell, a 5 mm distance between the shell and drivetrain, and a maximum thickness of the drive train of 40 mm (assuming a balanced mass distribution).

Additional wishes for the design are low manufacturing and material cost, controllability, safe materials and safe destruction.

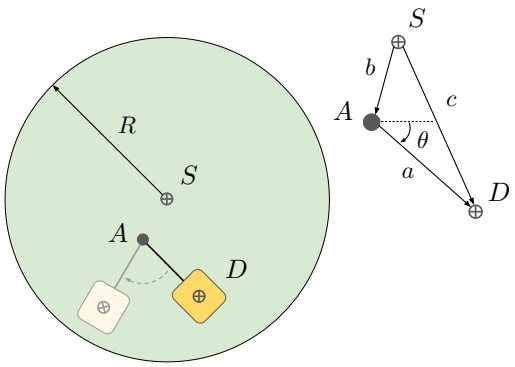

Fig. 3. Dimensions of fizzy, with S the center of the sphere, R the radius of the phere, A the fixed axis, D the center of gravity of the drivetrain, a the distance between A and D, b the distance between S and A, c the distance between S and D and θ the angle between a and the horizontal line.

2) Impact: The system must be robust against the playfulness of a child, i.e. the ball is able to withstand the maximum forces a child can impose on the ball. In this case study the force resulting from an 8-year-old is considered. To find the maximum force, an assumption is made on the worst-case scenario. It is assumed that kicking the ball will result in the highest forces compared to other interaction forces that can occur between the ball and the child.

According to literature, the maximum speed an 8-year-old can kick a ball ranges from 13.2 $\mathrm{m/s}$ to 13.6 $\mathrm{m/s}$ [32] [33] [34]. See Appendix B for the calculations on the ball speed. An overview of ball speeds and their corresponding forces can be seen in Table II. It is observed that the contact time, testing method, and ball speed have a great influence on the measured peak force. To get an estimate of the impact force, the worst-case scenario is assumed to be a ball kicked by a child instead of the ball hitting a wall. The maximum value measured by the kicking robot (1027 N) [35] forms the basis for the requirement for Fizzy.

The peak force is transferred back to a peak deceleration using the mass of the ball and Newton's second law, resulting in 2334 $\mathrm{m/s^2}$. With this deceleration an assumption is made that the connection between the shell and fixed axis from the drivetrain is rigid, resulting in an equal deceleration for both components. The final step to get the peak force imposed on the drivetrain is using the mass of the drivetrain and multiplying it with the deceleration. In a similar manner the maximum torque can be acquired, only taking an extra multiplication with the maximum moment arm ($\theta = 0$). See Table I for an overview of the requirements.

TABLE I
Design Requirements

Variable	Value	Unit
c	70	mm
R	100	mm
Mass	0.2	kg
Peak force	350	N
Peak torque	14	Nm

B. Design

The proposed solution for an impact resistant drivetrain in the robotic ball, combines a stretchable belt drive and a constant force mechanism (CFM). The belt drive has the function of the torque transfer between two parallel axis, the possibility to slip (torque limiter) and because it is stretchable, a series elastic actuation. On the other hand, the constant force mechanism complements the belt drive by keeping the belt tension constant even if the belt is stretched (realizing a reliable slip torque), as structural component to absorb the impact, and by providing sideways stiffness to enable the drivetrain to hold a horizontal position ($\theta = 0$ in Fig. 3).

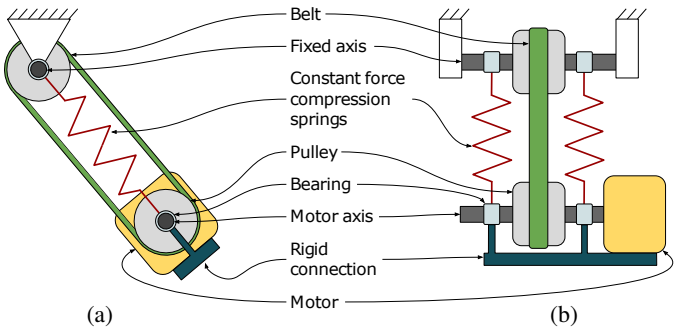

Fig. 4. Working principle of the belt drive. (a) Side view of the belt drive. (b) Front view of the belt drive.

1) Belt drive: The peak torque that the drivetrain can withstand is limited by the gearbox of the motor. The minimum torque is governed by the weight of the drivetrain and the distance between the fixed axis. With the peak and minimum torque, a region can be defined in which the torque must be transferred but not slip. The parameters that influence the slip torque are the friction coefficient between the pulley and belt, the pretension of the belt, the wrap angle of the belt around the pulley, the pulley diameter, and pulley geometry.

TABLE II
CHARACTERISTIC BALL IMPACT

Reference	Ball speed (m/s)	e (CoR)	Contact time (m/s)	Ball pressure (bar)	Peak force (N)	Ball weight (g)	Testing method
[36]	14	0.825	7.5	0.9	-	-	Finite element model
[37]	14	-	8	0.9	2362	426	Ball impact on force plate
[38]	15	0.835	8.2	0.9	2600	444	Ball impact on force plate
[39]	5.94	0.824	9.33	0.7	1117	-	Ball impact on force plate
[35]	15	-	13	-	1027	440	Force plate impacted on ball (kicking robot)
[40]	24	-	10.7	0.686	1610 ◇	434.8	high speed camera (human kick)
[41]	29.3	0.76	9	0.882	2926	430	high speed camera (human kick)

◇ Calculated peak force, the measured average force is multiplied by $\pi/2$, as stated in the paper.

In Appendix C influence of these parameters on the slip torque and mass distribution is shown. The dimensions of the pulley diameter and groove types are based on the available material, manufacturing possibilities, and their influence on the slip torque. The same holds for the different belt options. Since the friction coefficient is the most influential, different belt materials as well as pulley materials are considered to find the best combination that fits the slip conditions.

2) Constant force mechanism: An overview of a specific selection of constant force mechanisms is illustrated in Fig. 5. These mechanisms distinguish themselves from other constant force mechanisms by being passive, working in compression, and handling multiple impacts. In this study the inherent constant force mechanism (Fig. 5d) is most suitable for the robust drivetrain. The inherent constant force mechanism is compact, adjustable, low in weight, and can be made out of one part. A more detailed overview of the possible CFM that can be used in multiple impact scenarios can be found in Appendix A.

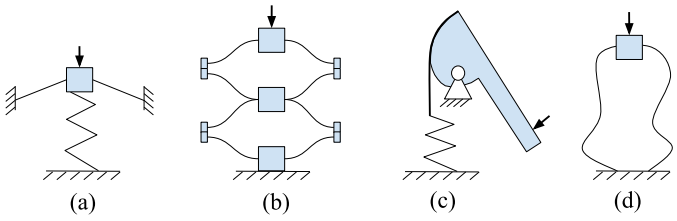

Fig. 5. Overview of constant force mechanisms that can handle multiple impacts. (a) Combination of negative and positive stiffness, (b) Negative stiffness elements in series, (c) Linear spring combined with a varying lever arm, (d) inherent zero stiffness.

C. Model for shape optimization

The model for the inherent CFM is based on the paper from Radaelli and Herder [42]. The model uses an isogeometric, geometrically nonlinear Bernoulli beam, with a linear material constitutive law. The model is adapted to accommodate the design requirements of Fizzy. The design is defined as a B-spline with 6 control points, as shown in Fig. 6. The whole system is made symmetrical around the center line $x = 0$, to ensure a straight movement up and down and to save on computational time. The locations of the control points are shown in Table III. Choosing two control points at the end instead of one enables a smooth sideways connection to the output. The spline is further divided into 50 nodes following the example of Radaelli and Herder [42].

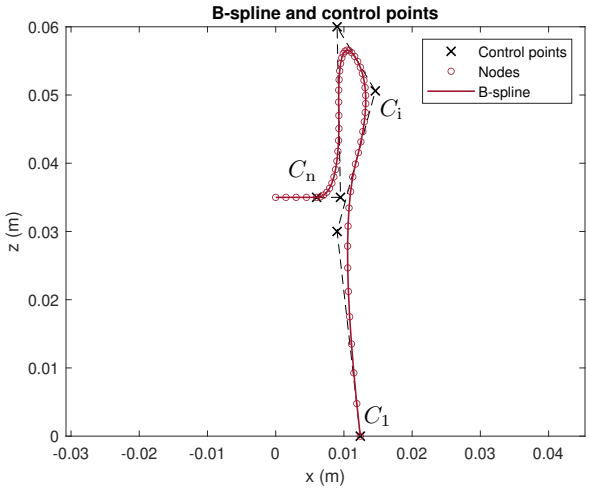

Fig. 6. Half of the shape of the constant force mechanism. With C_n control points where $n = 6$ and 50 nodes divide the B-spline. The layout of the figure is adapted from the paper by Radaelli and Herder [42]

A rectangular profile for the spline is chosen, because of its ease of manufacturing and scalability. The width and thickness can be adjusted to increase or decrease the constant force without having a large impact on the overall shape of the force profile [42]. An optimal design can be found by changing the thickness of the spline with every beam segment. However, this will increase the computational time significantly, since it will add 50 new variables to optimize. For this prototype, the thickness is set to one value over the entire length of the spline except for the end sections. The end section is thicker because this will hold the connection to the axis. The selected values for the thickness and width are 3 mm and 10 mm respectively.

The deformation of the design is modeled by setting a displacement of 15 mm on the end node. The first node is fixed and cannot rotate or translate. The end is only restricted in rotation because the mirrored other half of the mechanism will counter the rotational forces. The optimized design and how it deforms are shown in Fig. 7.

The main goal of the model for the constant force mechanism is to find an optimized design that exhibits constant force

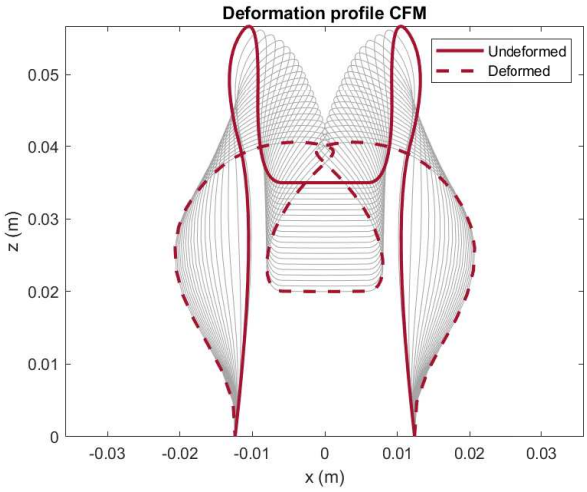

Fig. 7. Deformation profile CFM, sequence of 20 steps with a total compression of 15 mm, applied at the middle node of the mechanism. The undeformed and deformed configurations mark the beginning and end of the compression.

TABLE III
CONTROL POINTS OPTIMIZATION

Control points (mm)	Variables	Lower bound	Upper bound	Optimized values
C_{1x}	q_1	6	15	12.4
C_{1y}	0	-	-	0
C_{2x}	q_2	9	60	9
C_{2y}	q_3	0	30	30
C_{3x}	q_4	9	60	14.6
C_{3y}	q_5	20	60	50.6
C_{4x}	q_6	9	60	9
C_{4y}	q_7	20	60	60
C_{5x}	q_8	9	60	9.5
C_{5y}	35	-	-	35
C_{6x}	6	-	-	6
C_{7y}	35	-	-	35

over a large range of motion. Therefore, the objective function that is used for the optimization should minimize the error between the prescribed ideal CFM and the proposed design. A way of comparing the two mechanisms is by looking at their potential energy functions. A constant force spring has a linearly increasing potential energy function, which is not the case for a non-ideal CFM. Taking the normalized sum of the squared errors between the ideal energy function and the normalized energy function, results in the following objective function

$$f = \frac{(\tilde{U} - \hat{U})(\tilde{U} - \hat{U})^T}{\hat{U}\hat{U}^T}, \tag{1}$$

with $\hat{U}$ the reference energy of the ideal CFM and $\tilde{U}$ the normalized potential energy of the design that has to be optimized. The objective function and the derivation can be found in more detail in the paper by Radaelli and Herder [42].

An extra constraint is added to the optimization to increase the probability of a feasible design. By constricting the minimum distance between nodes, sharp edges and loopings are less likely to occur. The constraint follows the following formula for a negative null constraint: $g = d_{\min}/d_{\text{nodes}} - 1$. With $d_{\min}$ the minimal distance between the nodes and d_{nodes} the calculated distance between the nodes. The optimization is run using 50 random starting points with the MultiStart option in the Global Optimization Toolbox in Matlab. The optimization algorithm implemented is Sequential Quadratic Programming. The variable's lower and upper bounds as well as the extra constraint are added to the optimization and the results of the optimized control points are given in Table III.

D. Testing

1) Material choice: The combination of different belts, pulley materials, and pulley geometries is tested to find out if there is an optimal solution for the slip conditions of the drivetrain. The available belt materials are two types of o-rings, Nitrilbutadieenrubber (NBR) with shore hardness 70 and 90, and a stainless steel garter spring. The pulley materials and geometry are bound by the manufacturing capabilities. The manufacturing options available for this study that can create high strength and roundness are a Formlabs SLA printer and a lathe. The materials used for the pulleys are Grey Resin (Formlabs, USA) [43] and Aluminium 7075. The pulley geometries that can be made on a lathe are flat, 55 deg, and 35 deg v-grooves. For comparison, the same geometries are used for the Grey Resin pulleys. An overview of the different belts and pulleys can be seen in Fig. 8.

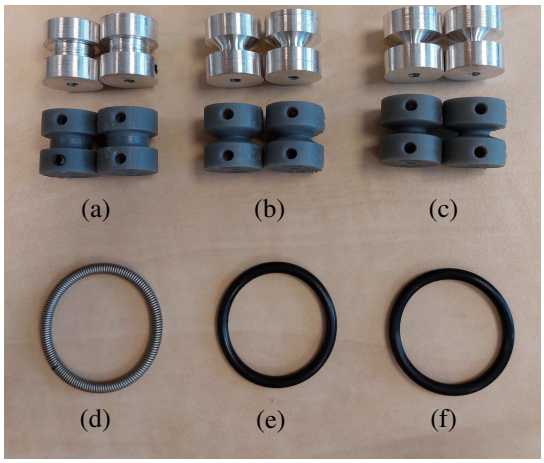

Fig. 8. Different pulleys and belts. (a) flat pulley, (b) 55 deg v-groove pulley, (c) 35 deg v-groove pulley, (d) Stainless Steel garter spring, (e) NBR shore 70, (f) NBR shore 90.

2) Test specifications: In order to get an overview of the characteristics of the different belt materials three tests are performed: tension, cyclic loading, and creep. Important parameters that follow from the tests are the yield strength, the hysteresis curve, and settling time. The belt characteristics together with the slip conditions can be used to find an optimal design.

To compare the CFM model with a physical prototype a CFM out of Thermoplastic Polyurethaan (TPU) is printed. The TPU is chosen mainly due to its elasticity and ease of manufacturing. However, a downside of 3D printing is the

variety in stiffness. To overcome this, a dogbone tensile test is conducted to find the Young's Modulus of the specific 3D-printed TPU. Following the example of Xu et al. [44], the Young's modulus is found by testing a dogbone profiles as indicated in standard ISO37 [45]. The dimensions and geometry of the dogbone, as well as the testing conditions, can be found in Appendix D.

3) Test setup: Two different test setups are used to measure the belt and pulley characteristics and to validate the CFM model. The first test setup is illustrated in Fig. 9. It consists of two parallel axes mounted straight above each other. The lower axis is fixed and cannot rotate, while the upper axis is supported by bearings and can be rotated with the leverarm. The fixed axis is mounted on a linear guide and can therefore only move vertically up and down. The two axes are connected via a belt and two pulleys. The pretension in the belt can be set to a desired value by applying weights to the lower axis. In a similar manner the torque on the rotating axis can be applied, only here the weights are applied at the end of the leverarm. Two pointers are attached to the setup to indicate the middle of the two axis, and in combination with a caliper, the exact elongation of the belt can be measured. Alternating the pulley and belt material as well as the weight combinations will lead to different testing scenarios. The tests performed with this test setup are the creep test of the different belt materials and the slip torque test.

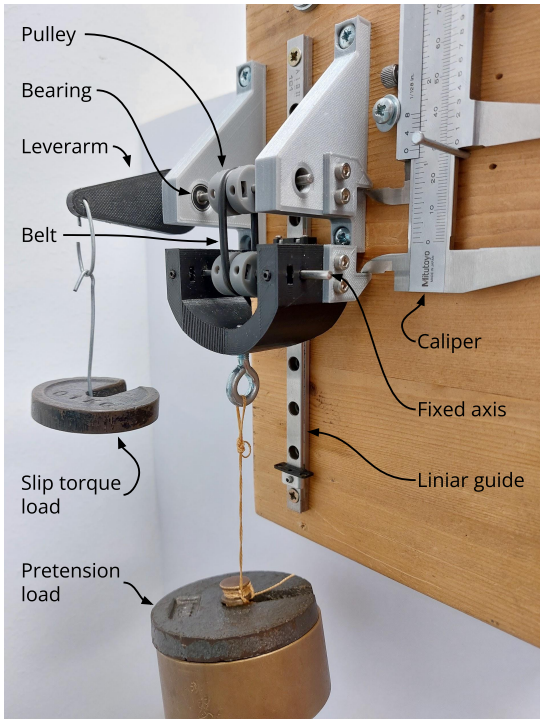

Fig. 9. Test setup, with NBR o-ring as belt and Grey resin pulley. The construction parts connecting the fixed and rotating axis as well as the leverarm are all from 3D-printed PLA. The complete test setup is mounted on a wooden block.

The second test setup is a ProLine Z010 (ZwickRoell, NL) [46], with a 500 N load cell. This is a universal test bench, which has a high stiffness and precise guidance of the load cell. The samples can be placed inside the test setup with a gripper or in case of a compression test between two parallel blocks. This test bench is used for the tensile test on the dogbone and belt materials, the compression test of the CFM, and the cyclic loading of the belts. The tests are executed following the protocol in Appendix D, taking into account the safety regulations the test setup requires.

4) Case study: To investigate the size, mass, and mass distribution of the proposed design a functioning prototype is built. The prototype uses a similar battery to the previous prototype of Fizzy, Lithium Ion INR18650 MJ1 3500mAh (LG Chem, Korea) [47]. Also, the PCB design holds the same components only changing the configuration to fit the form factor of the new design. For the actuation of the drivetrain, the servo motor TS90M Micro servo 360°ANALOG (TIANKON-GRC, China) is used [48]. This servo is inexpensive and has the required torque and speed specifications. Additionally, the gearbox is made from metal gears increasing the maximum torque the servo can handle. The complete prototype will be used to validate the mass distribution by measuring the mass and lengths between the fixed axis and center of gravity of the drivetrain. The minimal torque requirement and speed are tested by setting the maximum speed on the speed controller and measuring the number of rotations per minute. With the drivetrain initial impact resistance can be demonstrated. By statically compressing the drivetrain an indication of its ability to absorb impacts is felt.

III. Results

A. Belt characteristics

The tensile test of the belt shows a clear difference in stiffness between the three belts. With NBR Shore 90 showing the highest stiffness over the whole displacement. The tensile test is shown in Fig. 10. The breakpoint of the two NBR belts is around the same force. Whereas the SS Tension spring does not fail within the given displacement. The test is stopped prematurely at 150 mm displacement. It is clear that the belt will follow the trend of plastically deforming until the spring is completely stretched. The test setup is not capable of such a large displacement and the extra data is not required to make an assesment on the tensile behaviour of the belt.

In Fig. 12 the cyclic loading test is shown. The first loading cycle of the NBR belts shows a different behaviour compared to the following cycles. A stiffer response is seen, and in the case of NBR Shore 70 the response is also more linear. The hysteresis curve is visible in all belt types, with the SS tension spring having the smallest hysteresis curve. Similar to the findings from the tensile test, the NBR Shore 70 belt shows a clear increase in stiffness at around 30 N.

The results of testing the creep in the NBR o-rings are shown in Fig. 12. The NBR Shore 70 and 90 both settle at around 6 percent elongation. With an initial length of 35 mm, the resulting elongation is 2.1 mm. The initial length of the belt is taken directly after loading and is measured between the two axes in the test setup as shown in Fig. 9.

B. Friction between belt and pulley materials

The result of the friction test is seen in Fig. 13. The feasible region where enough torque can be transferred but

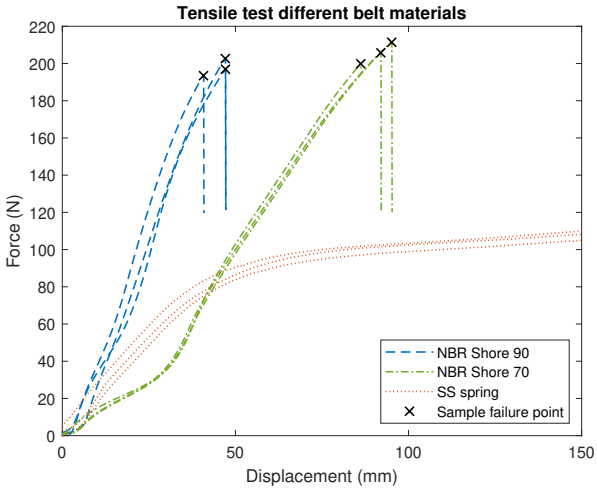

Fig. 10. Stiffness comparison between (NBR) Nitrilbutadieenrubber Shore 70, Shore 90 and (SS) Stainless Steel tension spring . De length of the belts are all set to 26 mm in diameter

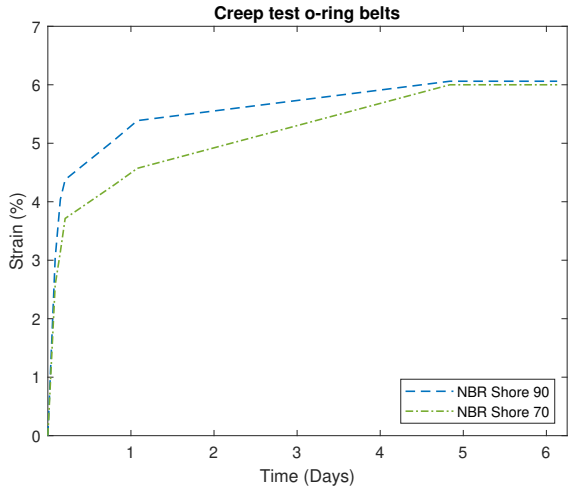

Fig. 12. Creep test of an o-ring (NBR) Nitrilbutadieenrubber Shore 90 and 70. The diameter of the o-rings are 27 mm and the constant load during the testing phase was 2 kg

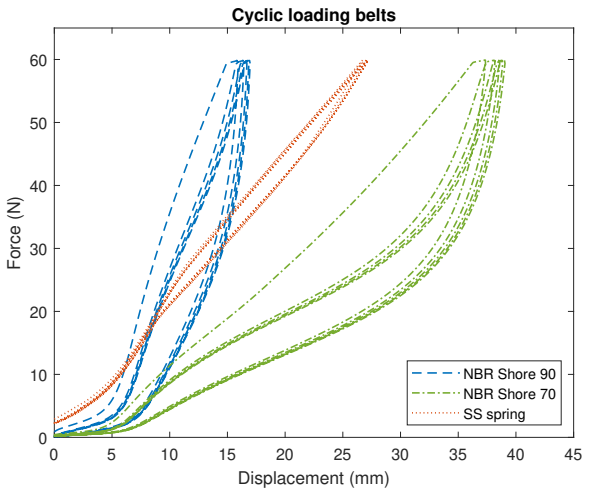

Fig. 11. Cyclic loading comparison between (NBR) Nitrilbutadieenrubber Shore 70, Shore 90 and (SS) Stainless Steel tension spring. De diameter of the belts are all set to 26 mm

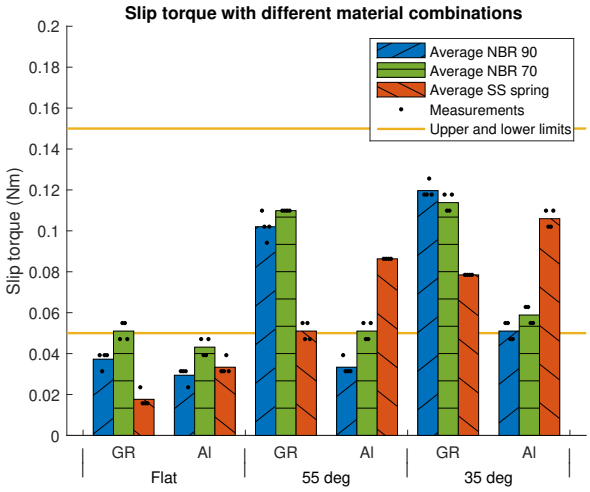

Fig. 13. Slip torque of the different belt types and pulley materials. Pulley geometry: (flat) flat surface contact with the belt, (55 deg) v-groove with an angle of 55 degrees, and (35 deg) v-groove with an angle of 35 degrees. Pulley materials: (GR) Grey Resin and (Al) Aluminium.

does not overload the motor is marked by the upper and lower limit lines in the graph. The measurements are taken with increments of 0.0078 Nm, resulting in the discrete steps as seen in the graph. The maximum standard deviation of the measured combinations is 0.0039 Nm,

The combination of Stainless Steel with Aluminium has a higher slip torque value compared to the combination with Grey resin. This is the other way around with the NBR belts. The NBR belts have higher slip torques with the Grey resin pulleys compared to the Aluminium ones. The trend that spans all combinations is the increase in slip torque with decreasing v-groove angle.

The highest average slip torque, of 0.120 Nm, is measured with the 35 deg Grey resin pulleys in combination with an NBR Shore 90 belt.

C. TPU Constant force mechanism

The tensile test with the dogbone samples is shown in Fig. 21. The dogbone samples show a large deformation path of which only the first segment is completely elastic. The average Young's Modulus over this elastic region is 50 Mpa. The Matlab model is adjusted with the Young's Modulus found by the dogbone tensile test. The model together with the measurements of the TPU compression test are shown in Fig. 15. The model shows a similar trend as the TPU Undeformed for the first part of the compression this is not the case for the TPU deformed for 1 day and 2 weeks. The TPU shows a decreasing trend in force when compressed for a longer period of time. The force at the desired displacement drops from around 19 N to 10 N when compressed for 2 weeks.

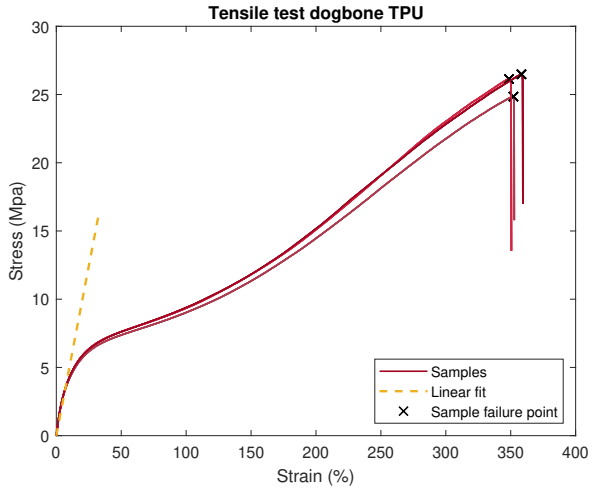

Fig. 14. Dogbone tensile test with 3 samples. The linear fit is fitted on the initial elastic region of the dogbone samples.

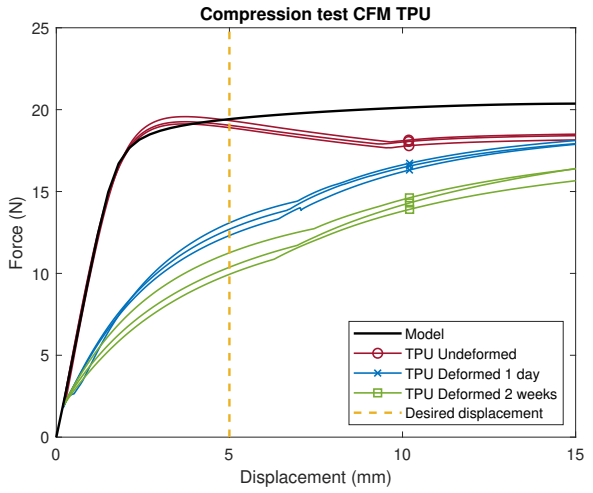

Fig. 15. Comparison between the model of the CFM and the 3D-printed TPU. Three different sets of TPU are tested in compression. The undeformed TPU has not been deformed before testing, whereas the deformed TPU have been compressed for 1 day and 2 weeks. The desired displacement represents the final compression length required in the complete prototype.

D. Final design

The final design is shown in Fig. 16. The prototype is connected via the fixed axis to a stand, enabling the drivetrain to rotate freely. The weight of the drivetrain is 142 g and the weight distribution matches the requirement to move the center of mass to the middle of the ball. Furthermore, the drivetrain is capable of rotating a full turn and has a maximum speed of 105 rpm. With continuous rotation at maximum speed, the current drawn by the motor is around 1 A. With this current draw the battery would last around 3.4 hours of continuous spinning. The prototype has the potential to absorb an impact without component failure. This potential is shown by the ability to compress the drivetrain in the direction of the fixed axis and by the compliance in torsion, bending, and stretching.

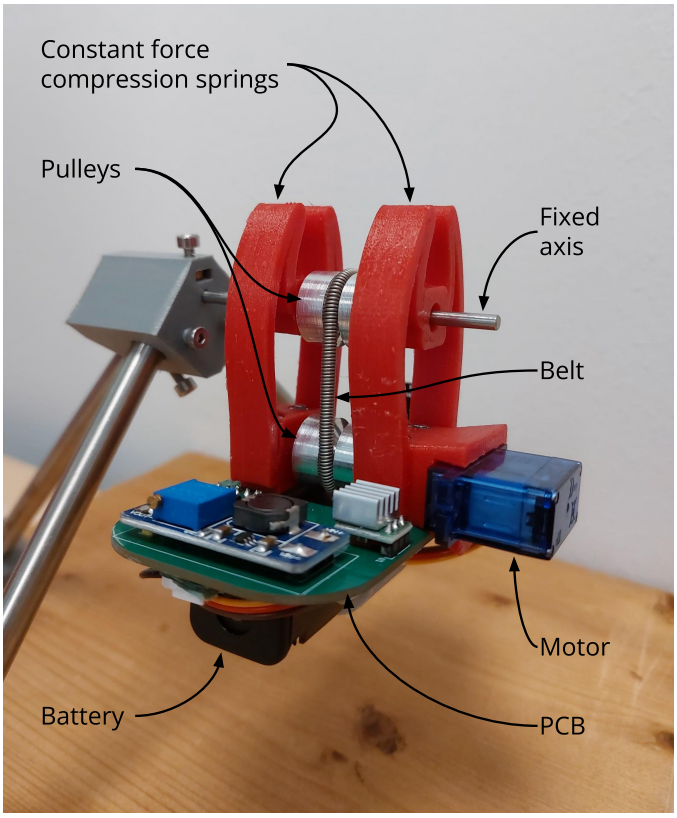

Fig. 16. The final prototype with integrated PCB and battery. The prototype is connected to a stand. The stand holds the fixed axis in place to allow rations of the drivetrain.

IV. Discussion

A. Main findings

The goal of this research is to design a drivetrain that can be implemented in the robotic ball, Fizzy and is impact resistant. The proposed design meets the weight and space requirements of the robotic ball. And an important feature of Fizzy, the 'folded' configuration, is also achieved with the proposed drivetrain. The masses and the locations of the drivetrain and fixed axis are balanced when folded, such that the centre of gravity is in the middle of the ball, resulting in a 'normal' rolling ball. The final design with motor, PCB and battery provides a platform, which can be used to implement and test control algorithms or sensors.

The proposed design shows great resistance against torque overload. The test on the slip torque shows the capability to handle torque overloads. But the impact mitigation of a direct hit is yet to be investigated, with the connections between the components assumed to be the most critical areas. The first step in the direction of a robust robotic ball is made with the proposed drivetrain.

B. Slip conditions belt drive

The belt drive's slip conditions ensure the drivetrain's robustness in torque overload. The belt will slip only when there is an excessive torque, in other situations it will have enough friction to transfer the torque of the motor and rotate the drivetrain around the fixed axis. The slip test shows several

combinations within the feasible range. However, a closer look at the conditions and characteristics of the slip torque test will show the importance of a slip torque close to the upper limit. Enhancing mobility has always fascinated me, together with a mechanical design aspect becomes a great motivator. Therefore, I'm grateful for this master thesis project and hopefully stimulate movement with the design made.

My thesis could not have worked without the help of my two supervisors, Heike Vallery and Marco Rozendaal. I would like to thank them both for their insights and feedback. Despite the difficulty of scheduling a meeting with them together, it was motivating to see how they balanced a good mixture of creativity and functional design.

Last year Heike introduced me to Giuseppe Radaelli. The meetings with Giuseppe were very helpful and would like to thank him for taking the time for my questions. Heike also introduced me to the DBL lab, which got me a new workplace, friends, and the organization of a cleanup day. I would like to express my gratitude to the people in the lab and a special thanks to Bob for the short feedback moments and fun in the office.

Lastly, I would like to thank my parents for their support and I would like to thank my girlfriend who can cheer me up as well as tell me to get to work and will always be in my mind. Over time the belt drive will be influenced by wear, this will most likely reduce the slip torque. Additionally, the sensitivity of the test with respect to a changing environment is high. The grease of a human hand or the initial lubrication of the NBR o-ring will decrease friction. Another limitation of the slip torque test is that the load is applied statically. With a dynamic change in applied load, the slip torque would decrease. These limitations show the importance of choosing a belt-pulley combination with a high slip torque.

An interesting behaviour is observed regarding the NBR o-rings in combination with the 35 deg v-groove pulleys. When loaded the NBR o-rings get wedged inside the pulley, to the point it is stuck and requires extra force to pull out, which lowers the efficiency of the drivetrain. Hence, a pulley with a larger v-groove angle is more favourable when combined with an NBR o-ring, especially with the negligible difference between the slip torques. Taking the pulley geometry and slip conditions into account, the following combinations are considered the best solutions according to the slip torque test: NBR Shore 70 with Grey Resin 55 deg pulley, NBR Shore 90 with Grey Resin 55 deg pulley, and the SS spring with Aluminium 35 deg pulley.

In this study, the slip conditions are not modelled but tested. To verify the experimental data a model could be made from the belt drive similar to the model proposed by Kong and Parker [49]. The proposed model uses creep theory with added belt bending stiffness to describe the state of a continuous belt drive. Adapting the model for sudden torque increases could result in an accurate model describing the belt drive and can be used for future adaptation to the belt drive.

C. Belt characteristics

1) Belt test results: The choice for the optimal belt material is made according to the stretch, cyclic loading, and creep tests. In general, a more predictable and stiff material is desired for the belt drive in Fizzy, because it will react faster and it is easier to model. The NBR Shore 90 shows these stretch characteristics as well as the SS spring. The stiffness of the NBR Shore 70 shows a clear nonlinear behaviour, with an increase in stiffness at around 30 N. This increase in stiffness is not observed with the NBR Shore 90 belts. A possible explanation could be a difference on the molecular level. NBR Shore 90 has a higherer degree of crosslinks between the elastomer chains compared to NBR Shore 70 [50]. The larger amount of crosslinks could prevent the initial movement of the elastomer chains and result in the behaviour seen in the tensile test.

In the cyclic loading test, the hysteresis in all belt materials is visible. The test shows that the SS spring has the best characteristics and would be preferable in a belt drive system. The reason is the low energy loss, which is the difference between the area's enclosed by the load and unload cycles. However, unexpected is the still visible amount of hysteresis occurring in the SS spring belt. The hysteresis could be due to the mounting of the spring in the test setup. A pulley is used, like in the final design, to stretch both ends. The friction between the belt and the pulley could cause the Stainless Steel spring to show the observed hysteresis.

The creep test shows the result of rubber being stretched over a longer time span. The result is similar to the cyclic loading test, the rubber has to settle first before it reaches a steady state. In the steady state, it could be used in an application, like a belt drive. The benefit of the SS spring is not having to deal with the settling time and no prediction has to be made on the final settling distance, as is the case with the NBR o-rings. With the goal of a durable design in mind, the NBR o-rings have another drawback. The ageing of NBR rubber results in more wear and lower tensile strength [51], because of these characteristics the belt has to be changed more often compared to a Stainless Steel option.

2) Final design: The final design uses a belt drive consisting of a Stainless Steel spring and an Aluminium pulley. These materials have the benefit of fast manufacturing and assembly, due to the fact that the SS spring can be opened and closed and the pulley can be precisely manufactured. The whole setup has a high repeatability rate because it does not have the uncertainty of the settling distance of NBR and the deviations in the 3D print quality of the Grey resin. An additional benefit is the increased efficiency of the SS spring with an Aluminium pulley over the use of the NBR o-rings.

D. Constant Force Mechanism

The proposed constant force mechanism fits inside the design size constrictions and is able to hold the drivetrain in place when it rotates around the fixed axis, which was the goal of the CFM. The tested TPU follows the model well for the first loading part (up to 2.5 mm), after which it deviates with a maximum of 2.1 N. The decrease in the compression force of the TPU could be linked to the decrease in Young's Modulus at higher strains. The model only takes into account a constant value, but the stiffness of the TPU material changes

with an increase in stress. Another reason for the discrepancy between the model and the TPU prototype could be the use of an isotropic homogeneous linear material model, which does not hold for the TPU prototype. For a better fit with the tested TPU CFM, a material model proposed by Holzweber et al. could be used [52]. Holzweber et al. analyze the properties of the TPU and converted them to a material model.

The TPU, like the NBR o-rings, has a tendency to relax when a constant load is applied. This can be seen in the compression test, where the compressed TPU of one day and one week are not comparable with the first load cycle and the model. The difference between the results from the deformed TPU of 1 day and 2 weeks shows a trend that could indicate that a steady state is reached after two weeks. However, further testing is needed to confirm this hypothesis. And similar to the NBR o-rings, a complete material model is needed to predict the deformed state after a given amount of time.

Overall, the TPU CFM does not show the desired constant force behaviour, but it holds the drivetrain in place and provides enough pretension at the desired displacement. The use in further prototypes could be justified by the ease of manufacturing and high adaptability of the material.

E. Future work

A recommendation for future tests is looking into the robustness over time. Wear, creep, and contaminated belt drive systems will influence the slip torque and impact capabilities. The system can be placed in a testing rig that holds the fixed axis in place and performs repeated impact tests. Testing in a real-world scenario would make the claim of a robust drivetrain stronger. But before the drivetrain can be tested in a real-world application the outer shell and the suspension between shell and fixed axis must be designed. The design of the outer shell and suspension will therefore be an interesting topic for future research. Inspiration can be derived from the design of the FIFA world cup ball, Al Rihla (ADIDAS, Germany) [53]. The ball has sensors inside that are suspended from the shell and are not noticeable to the players. The sensors weigh less compared to the proposed drivetrain, but a similar mechanism could be adapted.

With the drivetrain implemented in the robotic ball, improvements can still be made in the direction of an autonomous rolling ball. Implementing sensors that can detect the surroundings could be the first step. An extra feature of these sensors is proposed by Wensing at al. [27]. When the sampling frequency of the sensors is high enough, it is proposed that it can be used to mitigate incoming impacts. The result is a relaxed constraint on the impact resistance, potentially increasing the product's lifetime.

Other design modifications for future research on Fizzy could be to look at a low-geared motor and use the belt drive as a second transmission, not being 1:1 like the current version. A low-geared motor that is highly backdrivable could also potentially be used as a dynamo to regenerate energy. When designing a new combination of motor and gearbox, the design method proposed by Kojima et al. could be useful [54]. Kojima at al. studied the trade-off between a bigger motor with a smaller gearbox compared to a smaller motor with a bigger gearbox. Based on mass and power requirements an optimal design can be found.

Further research on the design of Fizzy is needed to achieve the final goal, a robust robotic ball that can autonomously roll and interact with the environment. The ball can be programmed to mimic different emotions and new features can be explored. For example, the ball can display happiness by making the ball jump, or sadness can be simulated by reducing the bounce of the ball when dropped. More features could be found in the playfulness of the child and designer. This approach creates an engaging platform that encourages and inspires children to be more curious and active.

V. Conclusion

In the pursuit of a sustainable design, an impact-resistant drivetrain is proposed. The drivetrain can handle torque overload and can be implemented in the robotic ball, Fizzy. The slipping feature of a belt drive in combination with a constant force compression spring makes a unique torque limiter and results in an economical and lightweight solution. Further research and development will be needed to finalize the design of Fizzy, fulfilling its potential to advance the field of robotic balls by making them robust. An important feature of robustness is not only prolonging the lifespan of the product but also impacting the feel of the ball. When considering the interaction with the product, the influence of the feel of the product, as well as the deformability of the product, play a vital role in shaping user experiences end perceptions. When the design purposefully incorporates deformability and tactile engagement, new products can be produced that not only stand the test of time but also resonate with the users on both practical and emotional levels.

Acknowledgments

The author would like to thank his supervisors Heike Vallery and Marco Rozendaal for their feedback and guidance. The author would also like to thank Giuseppe Radaelli for supplying the Matlab code and helping with the optimization of the constant force mechanism, Jan Frankenhuyzen for providing the material and advice on the mechanical assembly, Mascha Slingerland for the assistance with the Proline Z010 test setup, and Michael Fritschi for the PCB design and programming of the microcontroller.

References

[1] C. Boreham and C. Riddoch, "The physical activity, fitness and health of children," *Journal of Sports Sciences*, vol. 19, no. 12, 2001.
[2] I. Janssen and A. G. LeBlanc, "Systematic review of the health benefits of physical activity and fitness in school-aged children and youth," 2010.
[3] M. Lloyd, T. J. Saunders, E. Bremer, and M. S. Tremblay, "Long-term importance of fundamental motor skills: A 20-year follow-up study," *Adapted Physical Activity Quarterly*, vol. 31, no. 1, 2014.
[4] J. Sinclair, P. Hingston, and M. Masek, "Considerations for the design of exergames," in *Proceedings - GRAPHITE 2007, 5th International Conference on Computer Graphics and Interactive Techniques in Australasia and Southeast Asia*, 2007.
[5] Rotundus AB, "GroundBot." [Online]. Available: https://rotundus.se/
[6] Cheerble, "Wicked Ball SE." [Online]. Available: https://www.cheerble.com/en-eu

[7] Sphero Inc., "Sphero BOLT." [Online]. Available: https://sphero.com

[8] G. Kouvoutsakis, K. Baxevani, H. G. Tanner, and E. Kokkoni, "Feasibility of Using the Robot Sphero to Promote Perceptual- Motor Exploration in Infants," in *ACM/IEEE International Conference on Human-Robot Interaction*, vol. 2022-March, 2022.

[9] L. Boccanfuso, E. Barney, C. Foster, Y. A. Ahn, K. Chawarska, B. Scassellati, and F. Shic, "Emotional robot to examine different play patterns and affective responses of children with and without ASD," in *ACM/IEEE International Conference on Human-Robot Interaction*, vol. 2016-April, 2016.

[10] F. Michaud and S. Caron, "Roball, the rolling robot," *Autonomous Robots*, vol. 12, no. 2, 2002.

[11] F. Michaud, J. F. Laplante, H. Larouche, A. Duquette, S. Caron, D. Létourneau, and P. Masson, "Autonomous spherical mobile robot for child-development studies," *IEEE Transactions on Systems, Man, and Cybernetics Part A:Systems and Humans.*, vol. 35, no. 4, 2005.

[12] M. BujÅák, R. Pirník, K. Rástočný, A. Janota, D. Nemec, P. Kuchár, T. Tichý, and Z. Łukasik, "Spherical Robots for Special Purposes: A Review on Current Possibilities," 2022.

[13] R. Chase and A. Pandya, "A review of active mechanical driving principles of spherical robots," 2012.

[14] V. Crossley, "A literature review on the design of spherical rolling robots," *Pittsburgh, PA*, 2006.

[15] S. y. Choi, S. c. Hong, S. k. Park, and S. w. Jeong, "Effects of Diameter-to-thickness Ratio on Impact Energy Absorption Capability of CFRP Cylindrical Crash Box," *International Journal of Automotive Technology*, vol. 23, no. 6, 2022.

[16] S. Xiang, H. Gao, Z. Liu, H. Yu, and Z. Deng, "A novel active suspension gravity compensation system for physically simulating human walking in microgravity," in *2016 IEEE International Conference on Robotics and Biomimetics, ROBIO 2016*, 2016.

[17] S. Seriani, "A new mechanism for soft landing in robotic space exploration," *Robotics*, vol. 8, no. 4, 2019.

[18] H. Yang and L. Ma, "Multi-stable mechanical metamaterials by elastic buckling instability," *Journal of Materials Science*, vol. 54, no. 4, 2019.

[19] N. Lauzier and C. Gosselin, "Series clutch actuators for safe physical human-robot interaction," in *Proceedings - IEEE International Conference on Robotics and Automation*, 2011.

[20] J. F. Schorsch, "Compound planetary friction drive," *U.S. Patent*, no. 10,113,618, 2018.

[21] J. Smith, "Tolerance rings [motor-overload protection]," *IEEE Industry Applications Magazine*, vol. 8, no. 5, 2002.

[22] J. W. Smith, "The application of tolerance rings to provide shock overload protection in EPAS systems," in *SAE Technical Papers*, 2004.

[23] D. Myrgren, S. Weisbjerg, and D. Bergström, "Correct torque limitation and driveline optimization," in *AISTech - Iron and Steel Technology Conference Proceedings*, vol. 2, 2013.

[24] S. Zhang, S. Guo, Y. Fu, L. Boulardot, Q. Huang, H. Hirata, and H. Ishihara, "Integrating Compliant Actuator and Torque Limiter Mechanism for Safe Home-Based Upper-Limb Rehabilitation Device Design," *Journal of Medical and Biological Engineering*, vol. 37, no. 3, 2017.

[25] L. Jian and K. T. Chau, "Design and analysis of a magnetic-geared electronic-continuously variable transmission system using finite element method," *Progress in Electromagnetics Research*, vol. 107, pp. 47–61, 2010.

[26] M. C. Tsai, Y. C. Wu, C. T. Chan, P. Y. Cai, P. W. Huang, and M. H. Tsai, "Integrated Design of Magnetic Gear and Electric Motor for Electric Vehicles," in *2016 International Conference of Asian Union of Magnetics Societies, ICAUMS 2016*, 2018.

[27] P. M. Wensing, A. Wang, S. Seok, D. Otten, J. Lang, and S. Kim, "Proprioceptive actuator design in the MIT cheetah: Impact mitigation and high-bandwidth physical interaction for dynamic legged robots," *IEEE Transactions on Robotics*, vol. 33, no. 3, 2017.

[28] S. Yu, T. H. Huang, X. Yang, C. Jiao, J. Yang, Y. Chen, J. Yi, and H. Su, "Quasi-Direct Drive Actuation for a Lightweight Hip Exoskeleton with High Backdrivability and High Bandwidth," *IEEE/ASME Transactions on Mechatronics*, vol. 25, no. 4, 2020.

[29] G. Lv, H. Zhu, and R. D. Gregg, "On the design and control of highly backdrivable lower-limb exoskeletons: A discussion of past and ongoing work," *IEEE Control Systems*, vol. 38, no. 6, 2018.

[30] L. Peng, Z. G. Hou, L. Peng, L. Luo, and W. Wang, "Robot assisted rehabilitation of the arm after stroke: prototype design and clinical evaluation," *Science China Information Sciences*, vol. 60, no. 7, 2017.

[31] H. Matsuki, K. Nagano, and Y. Fujimoto, "Bilateral Drive Gear - A Highly Backdrivable Reduction Gearbox for Robotic Actuators," *IEEE/ASME Transactions on Mechatronics*, vol. 24, no. 6, 2019.

[32] L. H. P. Vieira, S. A. Cunha, R. Moraes, F. A. Barbieri, R. Aquino, L. d. P. Oliveira, M. Navarro, B. L. S. Bedo, and P. R. P. Santiago, "Kicking Performance in Young U9 to U20 Soccer Players: Assessment of Velocity and Accuracy Simultaneously," *Research Quarterly for Exercise and Sport*, vol. 89, no. 2, pp. 210–220, 4 2018.

[33] M. C. T. Teixeira and L. A. Teixeira, "Leg preference and interlateral performance asymmetry in soccer player children," *Developmental Psychobiology*, vol. 50, no. 8, pp. 799–806, 12 2008.

[34] D. F. Stodden, Z. Gao, J. D. Goodway, and S. J. Langendorfer, "Dynamic Relationships Between Motor Skill Competence and Health-Related Fitness in Youth," *Pediatric Exercise Science*, vol. 26, no. 3, pp. 231–241, 8 2014.

[35] A. Koizumi, S. Hong, K. Sakamoto, R. Sasaki, and T. Asai, "A Study of Impact Force on Modern Soccer Balls," *Procedia Engineering*, vol. 72, pp. 423–428, 2014.

[36] D. S. Price, R. Jones, A. R. Harland, and V. V. Silberschmidt, "Viscoelasticity of multi-layer textile reinforced polymer composites used in soccer balls," *Journal of Materials Science*, vol. 43, no. 8, pp. 2833–2843, 4 2008.

[37] T. Iga, H. Nunome, S. Sano, N. Sato, and Y. Ikegami, "Novel mathematical model to estimate ball impact force in soccer," *Sports Biomechanics*, pp. 1–17, 11 2017.

[38] Z. Taha and M. H. A. Hassan, "A reaction-force-validated soccer ball finite element model," *Proceedings of the Institution of Mechanical Engineers, Part P: Journal of Sports Engineering and Technology*, vol. 231, no. 1, pp. 43–49, 3 2017.

[39] Z. Taha, M. H. A. Hassan, and M. A. Aris, "The Efficacy of Impact-Absorbing Materials during Collision with a Soccer Ball," *Applied Mechanics and Materials*, vol. 440, pp. 363–368, 10 2013.

[40] J. L. Tol, E. Slim, A. J. van Soest, and C. N. van Dijk, "The Relationship of the Kicking Action in Soccer and Anterior Ankle Impingement Syndrome," *The American Journal of Sports Medicine*, vol. 30, no. 1, pp. 45–50, 1 2002.

[41] H. SHINKAI, H. NUNOME, M. ISOKAWA, and Y. IKEGAMI, "Ball Impact Dynamics of Instep Soccer Kicking," *Medicine & Science in Sports & Exercise*, vol. 41, no. 4, pp. 889–897, 4 2009.

[42] G. Radaelli and J. L. Herder, "A monolithic compliant large-range gravity balancer," *Mechanism and Machine Theory*, vol. 102, 2016.

[43] Formlabs, "Grey Resin." [Online]. Available: https://formlabs.com/materials/standard/#draft-resin

[44] T. Xu, W. Shen, X. Lin, and Y. M. Xie, "Mechanical properties of additively manufactured thermoplastic polyurethane (TPU) material affected by various processing parameters," *Polymers*, vol. 12, no. 12, 2020.

[45] International Organization for Standardization, "ISO 37: Rubber, Vulcanized or Thermoplastic. Determination of Tensile Stress-Strain Properties," 2022. [Online]. Available: https://www.iso.org/standard/68116.html

[46] ZwickRoell, "ProLine Z010." [Online]. Available: https://www.zwickroell.com/nl/

[47] LG Chem, "Lithium Ion INR18650 MJ1 3500mAh." [Online]. Available: http://www.lgchem.com

[48] TianKongRC, "TS90M Micro servo 360 ANALOG." [Online]. Available: https://www.tinytronics.nl/shop/en/mechanics-and-actuators/motors/servomotors/ts90m-mini-servo-1.6kg-continuous

[49] L. Kong and R. G. Parker, "Steady mechanics of belt-pulley systems," *Journal of Applied Mechanics, Transactions ASME*, vol. 72, no. 1, 2005.

[50] A. Tobolsky and H. Eyring, "Mechanical properties of polymeric materials," *The Journal of Chemical Physics*, vol. 11, no. 3, 1943.

[51] C. L. Dong, C. Q. Yuan, X. Q. Bai, X. P. Yan, and Z. Peng, "Tribological properties of aged nitrile butadiene rubber under dry sliding conditions," *Wear*, vol. 322-323, 2015.

[52] J. Holzweber, J. Müller, U. D. Çakmak, and Z. Major, "Characterization and modeling of the fatigue behavior of TPU," in *Materials Today: Proceedings*, vol. 5, no. 13, 2018.

[53] ADIDAS, "Al Rihla." [Online]. Available: https://news.adidas.com/football/adidas-reveals-the-first-fifa-world-cup--official-match-ball-featuring-connected-ball-technology/s/cccb7187-a67c-4166-b57d-2b28f1d36fa0

[54] K. Kojima, Y. Kojio, T. Ishikawa, F. Sugai, Y. Kakiuchi, K. Okada, and M. Inaba, "Drive-train design in JAXON3-P and realization of jump motions: Impact mitigation and force control performance for dynamic motions," in *IEEE International Conference on Intelligent Robots and Systems*, 2020.

[55] B. Horstman, "A review on constant force mechanisms for impact protection," Delft, 8 2023.

[56] A. Lees and L. Nolan, "The biomechanics of soccer: A review," *Journal of Sports Sciences*, vol. 16, no. 3, pp. 211–234, 1 1998.
[57] R. K. Jensen, "Changes in segment inertia proportions between 4 and 20 years," *Journal of Biomechanics*, vol. 22, no. 6-7, pp. 529–536, 1 1989.
[58] J.-M. Battini, "Co-Rotational Beam Elements in Instability Problems," Ph.D. dissertation, KTH, 8 2002.

APPENDIX A
LITERATURE STUDY ON CFM

An adaptation of the literature review on constant force mechanisms by Horstman is given in this section [55]. The relevant information for understanding constant force mechanisms is filtered out, resulting in a brief summary of passive multiple-impact constant force mechanisms.

A. Introduction to CFM

In order to avoid damage to an object a limit must be set to the amount of force it is exposed to. This is typically the aim of impact protection systems, which use a certain amount of displacement to absorb the energy and prevent system failure.

The amount of energy a spring system can absorb is equal to the area underneath the curve of a force-displacement graph. To illustrate this, three different systems are depicted in Fig. 17, with $F_{\max}$ the maximum force that can be exerted before system failure. Of the three systems, the non pre-loaded spring shows the least amount of energy absorbed (Fig. 17(a)). The pre-loaded spring can be designed to have a larger area, but with that comes a bigger system, due to the large pre-tension in the spring (Fig. 17(b)). The ideal behaviour of an impact protection system is depicted in Fig. 17(c), where the force is constant and just below the force threshold. Systems that exert such behaviour can also be called constant force mechanisms (CFM), which in this example almost doubles the energy absorption compared to the non pre-loaded spring

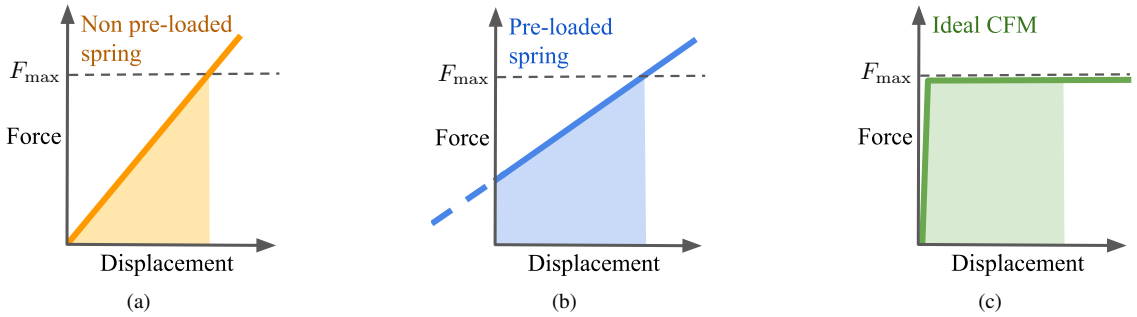

Fig. 17. Force displacement curves of different stiffness profiles, with the area under the curve being the energy absorption during deformation. (a) Non pre-loaded spring, (b) Pre-loaded spring and (c) Ideal CFM.

B. Categorization of CFM

For the categorization of CFM, a first distinction is made based on the model of a mass-spring-damper system. Only considering one degree of freedom, the formula for the equation of motion is given by

$$F = M\ddot{x} + C\dot{x} + Kx, \tag{2}$$

with the displacement of the system x, the external force F, the mass of the whole system M, the damping coefficient C and spring constant K. The model is illustrated in Fig. 18. The terms related to the design can be separated by acceleration, velocity, and deformation (right-hand side of equation 2). It is assumed that the mass of the CFM is neglectable compared to the mass of the electronics. Consequently, the velocity (further called rate) and deformation term are the only two characteristics of the design that can be altered to achieve a constant force mechanism.

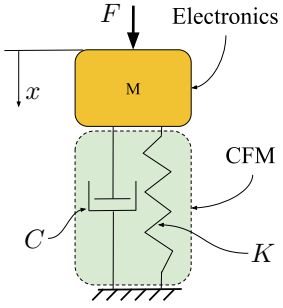

Fig. 18. Mass-spring-damper model of a protection system under impacting force F, modelled with a spring constant K and damper coefficient C. The mass of the CFM is neglected, compared to the mass of the electronics M. The system is compressed in positive x direction

The rate dependence can be achieved in two ways, by using viscous fluids or viscoelastic material. Since the rate-depending solution is not self-recovering on its own, it is not further considered this categorization. The same holds for the division of the deformation-dependent solutions, it can be divided into non self-recovering and self-recovering deformation. The latter is subsequently divided into passive and active designs. This distinction is made because the requirement for the robotic ball demands a passive system in order to make it lightweight and low on energy consumption. The last classification is based on the papers found in the literature search, where the difference is made in their geometric configurations with different construction elements.

C. Working principles

An overview of the working principles is given in Fig. 19. Based on the included papers the deformation depending, self-recoverable and passive solutions are divided into 4 methods. These methods all use different shapes and configurations to achieve constant force.

The first method combines a negative stiffness element with a positive stiffness element. By placing the different components in parallel, the stiffness is added up. This principle is used to approximate zero stiffness (Fig. 19(a)). In the ideal case, the stiffness would cancel out and result in a finite length of perfect zero stiffness. In the last part of the displacement, the overall stiffness increases significantly, because the two springs both have positive stiffness in this region. These designs consist mostly of fixed guided beams for the negative stiffness component. Their behaviour is well known and can therefore lead to precise force output. In the studies that use NS+PS, all designs show a planer solution to make a constant force mechanism.

The second method uses negative stiffness components and aligns them in series. This creates fluctuations in the output force but can be designed to be small in contrast to the overall force. The method relies on the snap-through behaviour of negative stiffness beams. A single beam will show limited impact absorption capabilities, but multiple layers form a fluctuating pattern that can be tuned to stay in a certain force region (Fig. 19(b)). The behaviour of the systems is changed by tuning the geometric parameters.

Standard linear springs can also be used in combination with a varying lever arm to construct CFM. The result of this method is a varying transmission between the displacement of the end-effector and the strain of the spring (Fig. 19(c)). The designed systems consist of large components with large stroke lengths. A drawback of these systems is the need for multiple components needing assembly and introduce high friction levels between them.

The last method is about the design of a single element configured to show a constant force region by itself, also called inherent zero stiffness. The element is shaped in a particular way to influence the force over the whole range of motion (Fig. 19(d)).

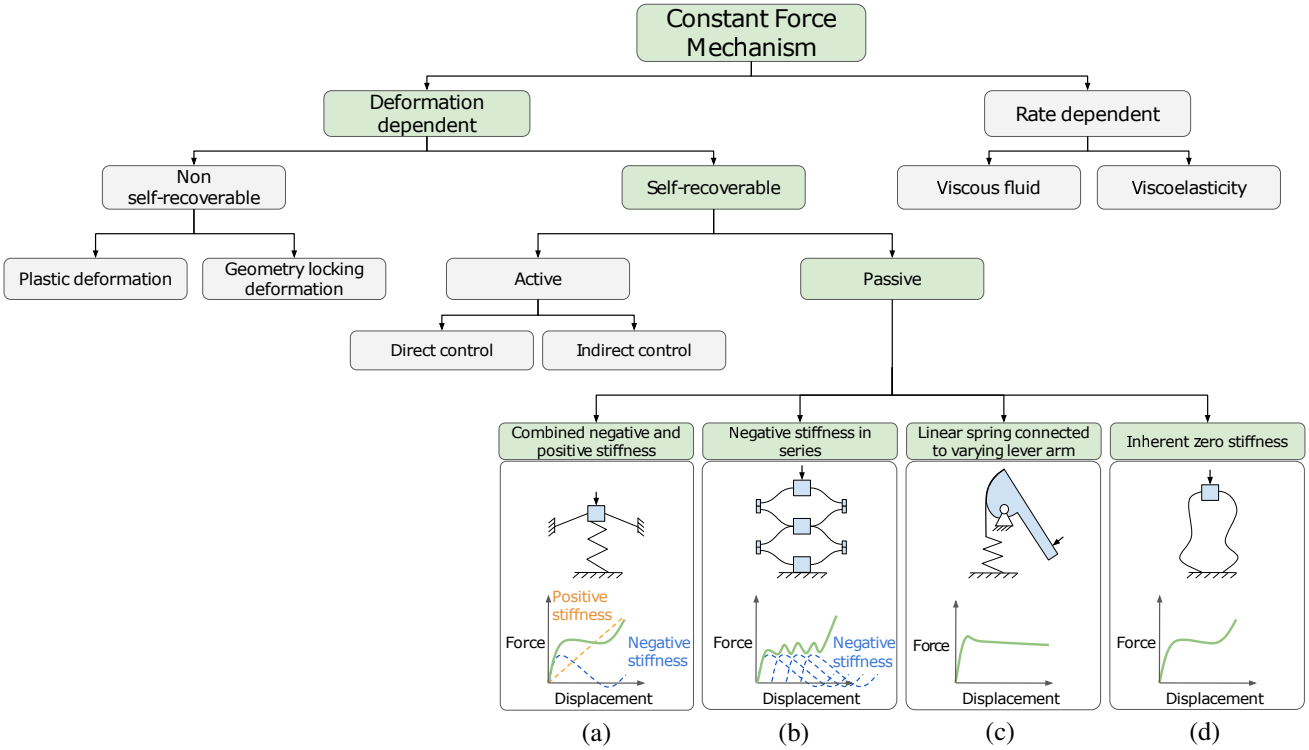

Fig. 19. Categorization of CFM. With (a) combination of negative and positive stiffness, (b) Negative stiffness elements in series, (c) Linear spring combined with a varying lever arm, (d) inherent zero stiffness.

APPENDIX B
CALCULATIONS ON BALL SPEED

Knowing the ball speed will enable finding similar ball speeds in impact tests reported in the literature. The result from impact tests with soccer balls is shown in Table II. Table IV shows the studies that report ball speed with the kick of a child. The found ball speeds are compared to the calculated ball speed for validation. The ball speed can be calculated with the formula for the Coefficient of Restitution (CoR) (3) and the conservation of momentum (4).

$$C_{\mathrm{r}} = \frac{|v_2 - v_1|}{|u_1 - u_2|}, \tag{3}$$

with C_{r} the CoR, v_1 and v_2 the speed of object 1 and 2 after impact, u_1 and u_2 the speed of object 1 and 2 before impact.

$$m_1 u_1 + m_2 u_2 = m_1 v_1 + m_2 v_2, \tag{4}$$

with m_1 and m_2 the mass of object 1 and 2, u_1 and u_2 the speed of object 1 and 2 before impact, v_1 and v_2 the speed of object 1 and 2 after impact. Separating the variable v_2 from (3) and substituting it in (4) results in the following equation,

$$m_1 u_1 + m_2 u_2 = m_1 v_1 + m_2 (C_{\mathrm{r}}(u_1 - u_2) + v_1). \tag{5}$$

Solving (5) for v_1 and rearranging the equation, the following equation can be derived,

$$v_1 = \frac{m_1 u_1 + m_2 u_2 + m_2 C_{\mathrm{r}}(u_1 - u_2)}{m_1 + m_2}. \tag{6}$$

The speed after collisions can be calculated with (6). The mass of the ball is that of a size 4 football, 0.375 kg. The striking mass of the leg is defined as the shank and the foot, with more stiffness in the leg the whole leg can be seen as the striking mass [56].

The mass of the impacting object is considered the whole leg of the child, assuming a stiff leg when the ball is impacted. Table V shows the percentage per body mass of the different parts of the leg. The mass of an 8-year-old according to Vieira et al is 30.1 kg [32]. The initial velocity of the foot is taken similarly to the study by Teixeira and Teixeira [33]. Lastly, an assumption is made on the CoR, considering it equal in the case of an impact on a force plate compared to a human kick. The average CoR found in TableII is 0.83. Entering the values in (6) results in a ball velocity of 13.36 $\mathrm{m/s}$. The result from the calculations compares to the found result in the literature. With these ball speeds an estimation on the impact force can be achieved. A sidenote must be placed on the speed that is taken as a reference point for the force on the ball. The studies that measure the velocity of the kick, the child is instructed to kick as hard as possible. This most likely not be the case in the robotic ball, resulting in a safety margin for the upper limit of the maximum ball speed.

TABLE IV
BALL SPEEDS OF CHILDREN (AGE 8)

Reference	v_foot (m/s)	v_ball (m/s)	# of participants	ball type
[32]	13.63	13.48	11	Outdoor ball size 4
[33]	8.6	-	8	Indoor ball size 4
[34]	-	13.6	84	Playground ball 20 cm ∅

TABLE V
WEIGHT OF THE LEG

Reference	Age group	Thigh ◇	shank ◇	Foot ◇	Total leg+foot (30.1 kg)
[57]	6 year old	0.095	0.05	0.02	2.10

◇ percentage of full body weight.

APPENDIX C
INFLUENCE DESIGN PARAMETERS

The influences on the slip torque of the preload and pulley diameter versus the friction coefficient are shown in Fig 20(a) and Fig. 20(b). It is seen that the friction coefficient between the pulley and belt has a greater influence on the slip torque compared to the preload and pulley diameter. This result shows the significance of testing the drivetrain on slip torque with varying material combinations. The region for a feasible solution is marked by the red lines. The upper limit is 0.15 Nm and the lower limit 0.05 Nm. The preload the CFM can produce is around 10 N per string. When lower values are used for the preload an increase in influence on the slip torque is seen. In this region the importance of a reliable constant force mechanism is clear. This is not the case for the pulley diameter, which stays more constant over the possible design region. The distance a is more sensitive to an increase in the weight of the fixed axis compared to an increase in the weight of the drivetrain, as can be seen in Fig 20(c). The pretension, torque, and slip torque are not influenced by the mass of the fixed axis. This makes it an ideal balance adjuster for tuning the system such that a folded configuration can be achieved.

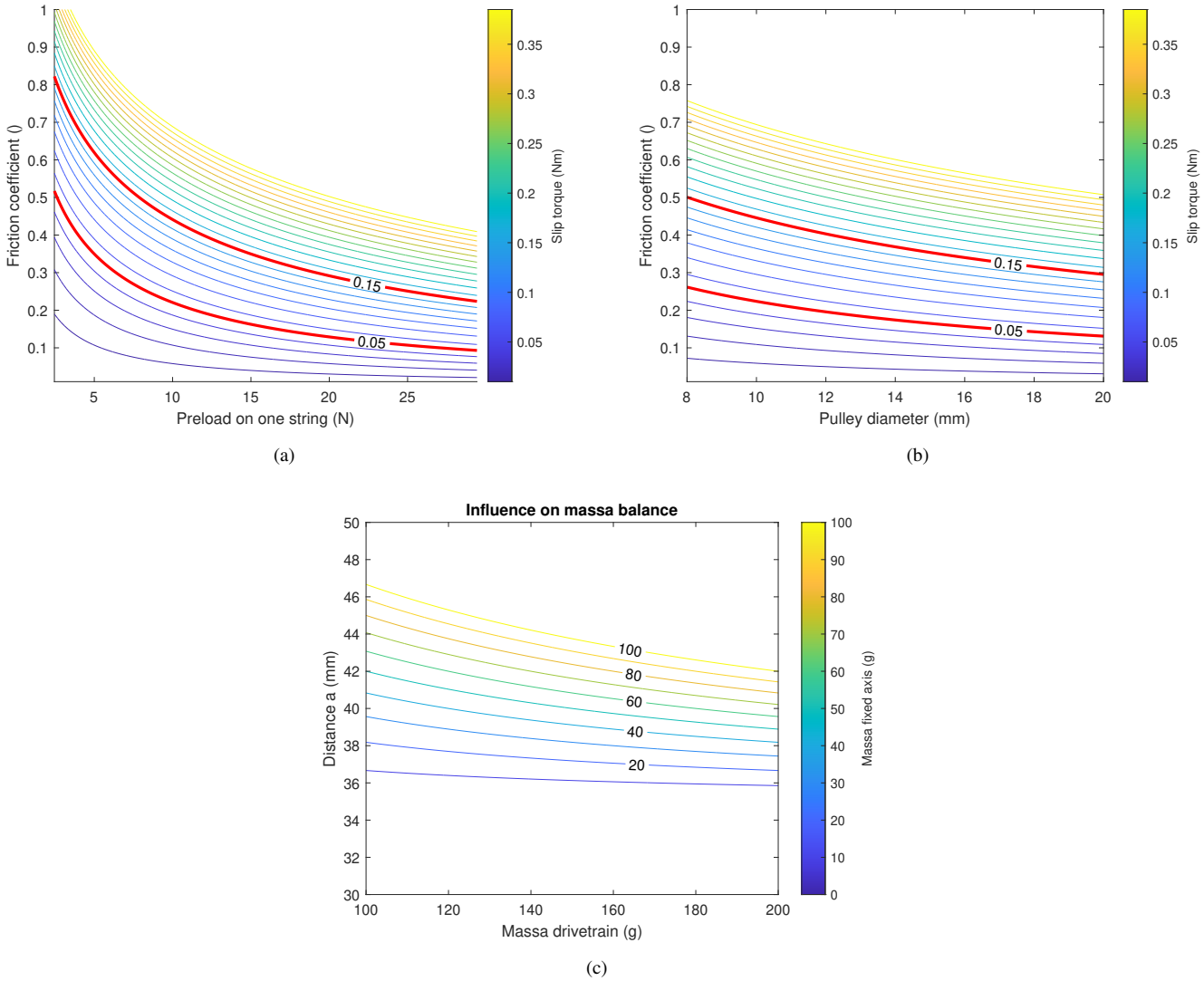

Fig. 20. (a) The influence of pulley diameter on the slip torque, (b) the preload on the slip torque and (c) the influence of the weights, of both drivetrain and fixed axis, on the the placement of the center of gravity of the drivetrain. The region for a feasible solution is marked by the red lines. The upper limit is 0.15 Nm and the lower limit 0.05 Nm.

APPENDIX D
TEST PROTOCOL

A. Tensile belts test

The belts are loaded until failure in the test setup. The test is bounded by a maximum force and elongation of 400 N and 150 mm respectively. This is done to prevent damage to the load cell or test setup. The speed is taken similarly to the dogbone test, 100 mm/min. The testing sequence is as follows:

1) Place the belt around the Aluminium pulleys and between the grippers from the test bench.
2) Set the safety glass in front of the test bench.
3) Start the tensile test.
4) Repeat 3 times for every belt type.

B. Cyclic loading test

The belt materials are all loaded until 60 N and then unloaded. The maximum load is chosen based on the findings from the tensile test. The interesting behaviour of the belts is considered in the region until 60 N and does not yield, hence the maximum force until which the belts are loaded. Test speed is similar to the dogbone test 100 mm/min. The test protocol:

1) Place the belt around the Aluminium pulleys and between the grippers from the test bench.
2) Set the safety glass in front of the test bench.
3) Start the cyclic loading test with 5 loading cycles.
4) Repeat for every belt type.

C. Creep test

An o-ring with a diameter of 25 mm is used to represent the final belt dimensions. 2 kg of weight as reload is taken to represent the constant force compression spring. The weight is based on the force feedback from the CFM when compressed to the desired length. Test protocol:

1) Place the belt around a pulley with a flat surface and in the test setup.
2) Apply the load to the fixed axis, pre-tensioning the belt.
3) Measure the elongation.
4) Repeat measurement keeping in mind the expected fast response in the first few hours and slower change after half a day.

D. Slip torque test

The slip torque test is performed on the test setup as shown in Fig. 9. The applied pretension on the belt is 2 kg, the same as for the creep test. The belt and pulleys are cleaned using a paper towel. This will ensure that no oil or grease is present from the manufacturer or from the testing person. The testing protocol is:

1) Place the belt around a pulley and in the test setup.
2) Apply the load to the fixed axis, pre-tensioning the belt.
3) Apply a weight to the leverarm in increments of 20 g.
4) After every increase in load, wait 30 s.
5) If the leverarm moves down in this time frame, note the weight of the previous load case as the slipping torque. unload the leverarm and turn the pulley and belt and repeat the loading sequence.
6) The whole cycle is done 4 times with every belt-pulley combination.

E. Dogbone test

The dogbone is tested as described in standard ISO37 [45]. The dimensions and geometry of the dogbone samples are illustrated in Fig. 21 and Table. VI. The speed of the test is set to 100mm/min and repeated 3 times. The same 3D-print settings are used for the printed dogbone as for the CFM. Settings: 80 percent infill with a Gyroid pattern, 230 °C print temperature, 0 °C print bed temperature, and a speed of 25 mm/s. Default settings for TPU95A from Ultimaker in the Ultimaker Cura program are used for the remaining settings. The testing protocol is:

1) Place the dogbone between the gripper with some extra sandpaper to increase the friction.
2) Set the safety glass in front of the test bench.
3) Start the tensile test.
4) Repeat for the three dogbone samples.

TABLE VI
DOGBONE DIMENSIONS

Dimension	Value (mm)
A	6
B	25
C	33
D	115
E (radius)	14
F (radius)	25
Thickness	2

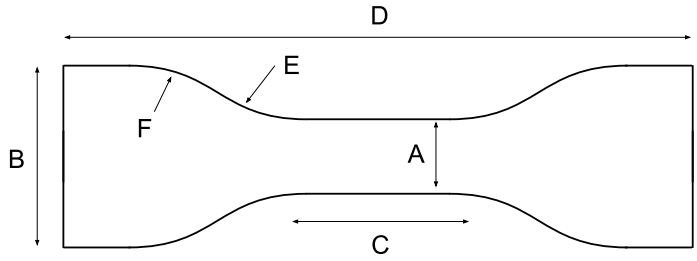

Fig. 21. dogbone test specimen

F. TPU compression test

The compression spring is combined with a holder before it is place inside the testing bench. The holder and the implementation in the test setup is shown in Fig. 22. The holder ensures the correct location where the force applies and keeps the spring in place. The CFM is loaded at a quasi-static rate of 5 mm/min, to minimize the effect of viscoelasticity. Nine TPU compression springs are loaded to their desired length (30 mm) and held in place with tie wraps. In pairs of three, they are compressed for two weeks, two days, and one day. The result can be compared with uncompressed TPU springs. The testing protocol is:

1) Place the CFM with holder between the compression blocks.
2) Set the safety glass in front of the test bench.
3) Start compression test.
4) Repeat for the nine CFM samples.

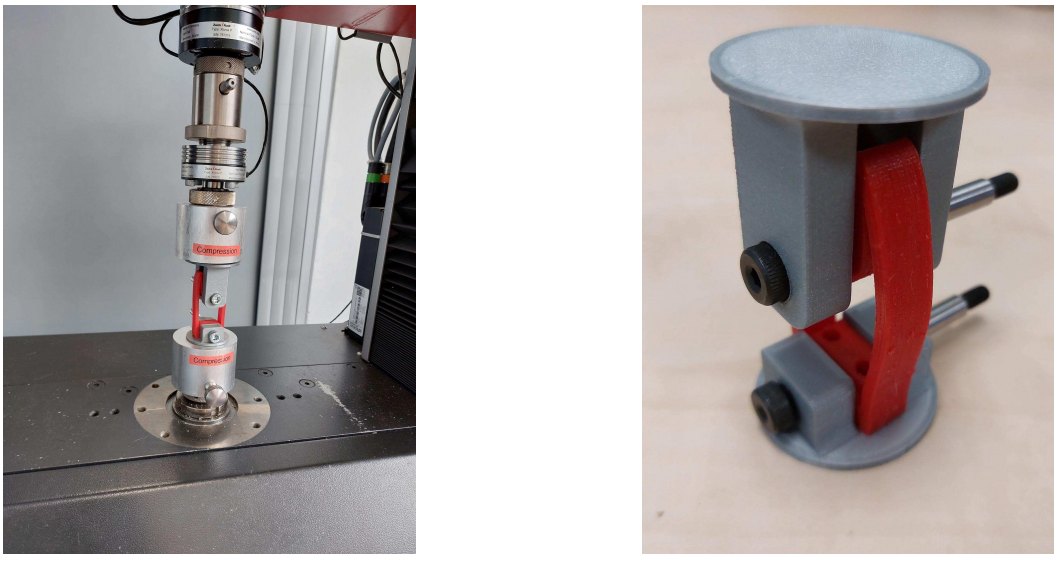

(a) (b)

Fig. 22. (a) The Proline Z010 with compression blocks and CFM in holder, (b) the CFM holder for compression test.

APPENDIX E
MATLAB CODE

Table VII, Table VIII and Table IX show the Matlab scripts that are used for this study. Table VII shows the scripts related to the Matlab code for data processing, Table VIII is a list of the scripts related to the Matlab code for shape optimization. These scripts use a Nonlinear 3D beam FEM script that cannot be shared. The original code is made by Battini [58] and access to the code is granted by Giuseppe Radaelli. Lastly, Table IX show the list of scripts used for calculations on the drivetrain parameters.

TABLE VII
MATLAB CODE DATA PROCESSING

Script name	Description
run_me.m	To run all scripts in this folder, displaying all figures
test_figures_tensile_belts.m	Tensile test of the three belt materials
test_figures_cyclic_loading_belts.m	Cyclic loading of the three belt materials
test_figures_creep.m	Creep test of the NBR o-ring materials
test_figures_slip_torque.m	Slip torque test results
test_figures_tensile_TPU.m	Tensile test of the dogbone samples
test_figures_comp_TPU.m	Compression test results of the CFM
CFM_spline_geometry.m	Settup of the CFM model geometry

TABLE VIII
MATLAB CODE CFM GEOMETRY OPTIMIZATION

Script name	Description
CFM_optimization.m	Optimization script to find the optimal shape of the CFM. The script uses a 3D beam FEM Matlab script: solveNONLINstaticCOR.m from Battini [58].
CFM_final.m	The complete design of the CFM is calculated and compared with the experimental data.

TABLE IX
MATLAB CODE DRIVETRAIN CALCULATIONS

Script name	Description
run_me.m	To run all scripts in this folder, displaying all figures
Belt_characteristics.m	Calculations on the influence of the belt parameters on the slip torque.
Influence$_massa_balance.m$	Calculations on the mass distribution of the drivetrain and fixed axis.
Impact_calculation.m	Calculations on the impact force and ball speed.